Engineering Analysis with Boundary Elements 169 (2024) 106025

Contents lists available at ScienceDirect

Engineering Analysis with Boundary Elements

journal homepage: www.elsevier.com/locate/enganabound

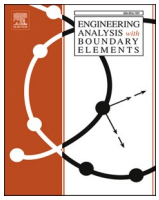

Fourth-order phase field modelling of brittle fracture with strong form meshless method

Izaz Ali [a], Gašper Vuga [a], Boštjan Mavrič [a,b], Umut Hanoglu [a], Božidar Šarler [a,b,*]

[a] Faculty of Mechanical Engineering, University of Ljubljana, Slovenia
[b] Institute of Metals and Technology, Ljubljana, Slovenia

ARTICLE INFO

Keywords:
Strong form meshless method
Fourth-order phase field
Crack propagation
Staggered approach, Polyharmonic Splines

ABSTRACT

This study aims to find a solution for crack propagation in 2D brittle elastic material using the local radial basis function collocation method. The staggered solution of the fourth-order phase field and mechanical model is structured with polyharmonic spline shape functions augmented with polynomials. Two benchmark tests are carried out to assess the performance of the method. First, a non-cracked square plate problem is solved under tensile loading to validate the implementation by comparing the numerical and analytical solutions. The analysis shows that the iterative process converges even with a large loading step, whereas the non-iterative process requires smaller steps for convergence to the analytical solution. In the second case, a single-edge cracked square plate subjected to tensile loading is solved, and the results show a good agreement with the reference solution. The effects of the incremental loading, length scale parameter, and mesh convergence for regular and scattered nodes are demonstrated. This study presents a pioneering attempt to solve the phase field crack propagation using a strong-form meshless method. The results underline the essential role of the represented method for an accurate and efficient solution to crack propagation. It also provides valuable insights for future research towards more sophisticated material models.

1. Introduction

In material science and structural engineering, cracks play an essential role by impacting the performance and integrity of materials. Griffith's groundbreaking contribution in 1920 [1] opened a new era of research in fracture mechanics by observing that crack propagation is a contest between increasing surface energy and releasing elastic energy. Generally, the numerical modelling of cracks can be divided into two categories, i.e., continuous/diffuse and discontinuous/discrete approaches. The discontinuous approaches involve a discontinuity in the displacement field [2], which is based on the well-known theories of linear elastic fracture mechanics (LEFM) and the cohesive zone model (CZM) [3]. It is challenging to model crack behaviour using discontinuous methods, such as crack initiation, nucleation, branching, propagation, and patterns [2], because the discrete methods need additional criteria to track the discontinuity in the displacement field explicitly [4]. The generalized finite difference method (GFDM) has been successfully applied to solve crack problems in anisotropic materials, demonstrating its accuracy and effectiveness through various numerical examples [5].

On the other hand, the diffuse methods, introduced in the late 1990s, have no discontinuity in the displacement field [2]. However, the stiffness degrades gradually as the damage increases. Some of the popular diffuse methods consist of the screened Poison method [6], gradient damage models [2] and phase field method (PFM) [7]. One of the most commonly used diffuse methods, PFM, is a robust and helpful approach because of its simple applicability in crack initiation, detection, and propagation. PFM does not require additional criteria for tracing the crack during propagation.

The PFM is a mathematical tool used to solve interfacial problems. This approach was used for the first time in the 1980s for modelling free-boundary problems [8]. The introduction of PFM to the analysis of cracks was first presented by Marigo and Francfort in 1998 [9] and is based on the approximate potential developed by Mumford and Shah [10] for image segmentation. This model was numerically implemented in 2000 [7]. Marigo and Francfort first considered predefined crack and crack paths [9], but later on, it was concluded that phase field (PF) could also detect crack initiation, and there is no need for predefined cracks [11]. The PFM is based on the variational principle of fracture mechanics, which is the generalisation of Griffith's theory. This principle embodies a broader conceptualisation, facilitating the demonstration of

* Corresponding author.
E-mail address: bozidar.sarler@fs.uni-lj.si (B. Šarler).

https://doi.org/10.1016/j.enganabound.2024.106025
Received 16 July 2024; Received in revised form 30 October 2024; Accepted 30 October 2024
Available online 6 November 2024

crack initiation and tracing crack propagation. In contrast to discrete methods, the global optimisation embedded in the variation principle in PFM allows the spontaneous emergence of each newly formed crack without specifying it in advance [12]. The differential governing equation of PF predicts crack propagation, whereas the length scale parameter in the PFM controls the shape of the crack [13]. Recently, PFM has been used for crack analysis in different fields, including brittle cracks [14–22], dynamic cracks [11,23,24], ductile cracks [25–28], cracks in composite materials [29–31], fatigue cracks [27,32,33], hydrogen assisted cracks [34–36] and others described in the review article [37]. The limitation of PFM is the computational cost due to the relation between the length scale parameter, which defines the thickness of the crack, and the node spacing [4]. For a numerically stable crack propagation, the minimum node spacing should be at least less than or equal to half of the length scale parameter [11].

The previously proposed second-order PF [11] is computationally expensive due to the requirement of highly dense mesh [4]. A fourth-order PF was proposed by Borden at al. [38], which consists of fourth-order derivatives of the PF parameter ϕ in the governing equation to loosen the mesh size requirements, regularise the PF and improve the convergence rate [13]. Due to the double Laplacian term ($\Delta^2\phi$) in the governing equation of the fourth-order PFM, the resulting PF solution exhibits high regularity, which ensures a smoother representation of the crack with no sharp discontinuities and provides a more precise depiction of the crack surface compared to the second-order PFM [39]. The results in [38] justify the fourth order being more accurate with a better convergence rate in terms of node spacing. In the context of the finite element method (FEM), the higher-order derivatives require a minimum of C^1 continuous basis functions [4], which are difficult to construct using FEM. To reduce the computational cost and provide a smooth and continuous discretisation in the domain, the authors in [4] used an adaptive h-refinement in the framework of isogeometric analysis (IGA). Many authors have contributed to fourth-order PF solutions for cracks using FEM, such as [40–45], weak form meshless isogeometric collocation method used in [13] and local maximum entropy approximant schemes used in [46].

The PF modelling of cracks has been done using commercially available software like COMSOL Multiphysics [47,48], ABAQUS [49–53] and open-source software FENICS [19,20,31] using the weak form of the governing equations in the framework of the FEM. These FEM-based tools are effective but face challenges, especially in large deformation problems and complex geometries.

Meshless methods, also known as mesh-free methods, offer a novel approach to numerical analysis by eliminating the need for a traditional mesh. Instead of relying on elements connected by nodes, these methods use a set of scattered/regular nodes to discretise the domain, which are free to move and adapt to changes in the problem geometry [54]. The meshless methods can be divided into weak-form and strong-form formulated. Despite good stability and accuracy, the weak-form meshless methods involve numerical integration, making them computationally more expensive [55]. The weak-form meshless methods have been successfully used for phase field modelling of crack propagation. For example, in [56], the weak-form meshless method is used for second-order PF brittle cracks, where a modified Newton-Raphson method is applied to restore the convergence of the radial point interpolation method iteratively. The Element-free Galerkin method is used for second-order PF modelling of cracks in [18] with h-adaptivity by triggering the refinement with the strain energy history, showing improved accuracy and computational efficiency compared to the case with no h-adaptivity. The isogeometric mesh-free collocation method is used in [13] to show the robustness and effectiveness of the fourth-order PF in terms of computational cost and crack surface resolution compared to the second-order PF. In [46], the authors used the mesh-free local maximum entropy approximation and showed that the fourth-order PF requires fewer nodes to resolve the crack path and has a more accurate crack surface than the second-order PF.

On the other hand, strong-form meshless methods directly discretise the partial differential equations without any need for integration. They are easier to implement numerically than the weak-form meshless methods and do not require any background mesh for approximation, making them computationally efficient [55]. The strong-form meshless methods offer simplicity and high boundary accuracy, while weak-form methods provide greater stability and flexibility [57]. However, the latter involves complex formulation. In [58], the authors propose a least squares radial basis function finite difference approach, based on the strong form meshless method, that improves stability and accuracy in solving partial differential equations, particularly on irregular domains, while maintaining the flexibility of meshless approaches. To this date, the strong-form meshless methods have never before been used for crack modelling using PF. Therefore, for the first time, this paper presents a solution procedure of a fourth-order PFM, solved with a strong-form meshless method, for crack propagation. One of the most popular strong-form meshless methods is the local radial basis function collocation method (LRBFCM) [54], also recently known as the radial basis function generated finite difference (RBF-FD) method. The LRBFCM employs local approximations within subdomains to calculate each node's local weights of differential operators. These locally computed weights are then used to construct a global stiffness matrix [55]. This feature of local approximations for LRBFCM makes it possible to solve large-scale problems compared to the global Kansa method [59]. A detailed overview and implementation of the LRBFCM can be found in the review article [60]. The LRBFCM has been used to successfully solve different problems, such as diffusion problems [54], advection-dominated problems [61], linear thermo-elasticity [62], h-adaptive LRBFCM [63], multi-pass hot-rolling simulation [64], numerical modelling of visco-plastic material [65], and the simulation of laminar backwards-facing step flow under a magnetic field with explicit LRBFCM [66]. The LRBFCM is used in [54] with multiquadrics (MQs) as an interpolation function, producing good results compared to the finite difference method (FDM) [54]. The main disadvantage of MQs is that they require a selection process for a suitable shape parameter [67]. Polyharmonic splines (PHSs) as radial basis functions (RBFs), on the other hand, involve a trivial formula for the selection of shape parameters [67,68]. This unique feature of PHSs in the RBF approaches has recently made it popular. PHSs also play a vital role in convergence, accuracy, and stability studies [69,70]. Another feature of PHSs is that they can deal efficiently with the numerical issues related to poor conditioning [71]. In [68] and [69], the authors reported that the number of nodes in the local subdomain must be at least twice the number of augmentation monomials to ensure h-convergence governed by the order of augmentation. Some recent notable research articles utilising PHSs include a coupled domain–boundary type meshless method for phase field modelling of dendritic solidification with the fluid flow [72], an improved local radial basis function method for solving small-strain elasto-plasticity [55], a hybrid radial basis function finite difference method for modelling two-dimensional thermo-elasto-plasticity [73], and its application to the metallurgical cooling bed problem [74]. An example of PHS use for reducing discretisation-induced anisotropy in the phase field modelling of dendritic growth is provided in [75].

2. Governing equations

The governing equations for the fourth-order phase field model can be derived from the regularised total potential energy $\boldsymbol{\Pi}$ of a body occupying a domain Ω with a boundary Γ, subject to prescribed boundary conditions [4].

$$\boldsymbol{\Pi} = E_e + E_s + E_{ext}, \tag{1}$$

$$E_e = \int_{\Omega} g(\phi)\psi(\boldsymbol{\varepsilon}) d\Omega, \tag{2}$$

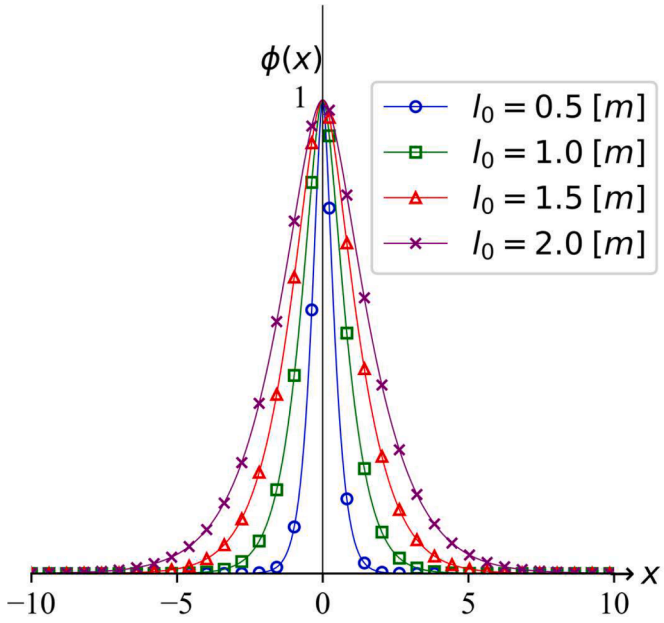

Fig. 1. Diffuse crack representation (Eq. (16)) in 1D for different length scale parameters.

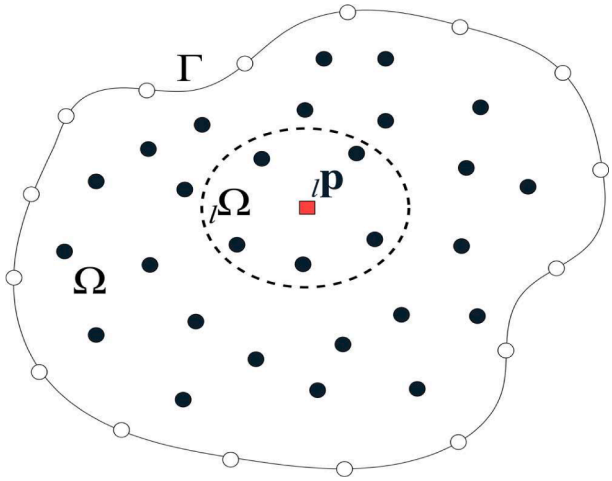

Fig. 2. Scheme of the domain Ω with boundary Γ. The solid and empty circles show the interior and boundary nodes, respectively. The dashed circular line shows the limits of a local sub-domain $_l\Omega$ containing six interior nodes. The solid square shows the central node $_l\mathbf{p}$.

$$E_{ext} = -\int_{\Omega} \mathbf{b}\cdot\mathbf{u}d\Omega - \int_{\Gamma} \mathbf{T}\cdot\mathbf{u}d\Gamma, \tag{3}$$

$$E_s = G_c\int_{\Omega} \gamma(\phi)d\Omega, \tag{4}$$

where E_e is the stored elastic energy, E_s is the surface fracture energy and E_{ext} is the external potential energy, $g(\phi) = (1-\phi)^2$ is the degradation function, $\psi(\boldsymbol{\varepsilon}) = \frac{1}{2}(\boldsymbol{\varepsilon} : \mathbf{C} : \boldsymbol{\varepsilon})$ is the strain energy density, $\mathbf{C}$ is the elasticity tensor, $\boldsymbol{\varepsilon} = \frac{1}{2}\left(\nabla\mathbf{u} + \nabla^T\mathbf{u}\right)$ is the strain tensor, $\mathbf{b}$ is the body force, $\mathbf{u}$ is the displacement and $\mathbf{T}$ is the prescribed traction on the boundary, G_c is the surface fracture energy, γ is the crack surface density and ϕ is the phase field parameter ($\phi = 0$ is intact and $\phi = 1$ is broken material). The crack surface density $\gamma(\phi)$ is defined as [4,38],

$$\gamma(\phi) = \frac{1}{2l_0}\left(\phi^2 + \frac{l_0^2}{2}\Delta\phi + \frac{l_0^4}{16}(\Delta\phi)^2\right), \tag{5}$$

where l_0 is the length scale parameter [76], used to regulate the diffusion of the crack. The surface crack energy Eq. (4) can be rewritten, by plugging in the Eq. (5), as

$$E_s = \frac{G_c}{2l_0}\int_{\Omega}\left(\phi^2 + \frac{l_0^2}{2}\Delta\phi + \frac{l_0^4}{16}(\Delta\phi)^2\right)d\Omega. \tag{6}$$

Putting Eqs. (2), (3) and (6) into Eq. (1) we get the total potential energy as

$$\boldsymbol{\Pi} = \int_{\Omega}\left[g(\phi)\psi(\boldsymbol{\varepsilon}) + \frac{G_c}{2l_0}\left(\phi^2 + \frac{l_0^2}{2}\Delta\phi + \frac{l_0^4}{16}\Delta^2\phi\right) - \mathbf{b}\cdot\mathbf{u}\right]d\Omega - \int_{\Gamma}\mathbf{T}\cdot\mathbf{u}d\Gamma. \tag{7}$$

By minimising the total potential energy in the Eq. (7) with respect to $\mathbf{u}$ and ϕ, we reach the strong form coupled balance equations for mechanical and PF models, respectively.

$$\nabla\cdot[g(\phi)\boldsymbol{\sigma}] + \mathbf{b} = \mathbf{0}, \tag{8}$$

$$\left(\frac{2l_0\psi(\boldsymbol{\varepsilon})}{G_c} + 1\right)\phi - \frac{l_0^2}{2}\Delta\phi + \frac{l_0^4}{16}\Delta^2\phi = \frac{2l_0\psi(\boldsymbol{\varepsilon})}{G_c}, \tag{9}$$

where $\boldsymbol{\sigma} = \lambda tr(\boldsymbol{\varepsilon})\mathbf{I} + 2\mu\boldsymbol{\varepsilon}$ is the stress tensor, λ and μ are Lamé parameters, whereas $\mathbf{I}$ is the second-order identity tensor and the corresponding boundary conditions ($\Gamma = \Gamma_u \cup \Gamma_T \cup \Gamma_F$) are

$$\mathbf{u} = \overline{\mathbf{u}} on \Gamma_u, \tag{10}$$

$$g(\phi)\boldsymbol{\sigma}\cdot\mathbf{n} = \overline{\mathrm{T}} on \Gamma_T, \tag{11}$$

$$\{u_n, T_t\} = \{0, 0\} on \Gamma_F, \tag{12}$$

where $\overline{\mathbf{u}}$ is the prescribed displacement at Γ_u, $\overline{\mathrm{T}}$ is the traction at Γ_T, and Γ_F is a free-slip boundary condition in which the body is restricted from moving in the normal direction $u_n = \mathbf{u}\cdot\mathbf{n} = 0$ and free to move in the tangential direction $T_t = \overline{\mathrm{T}}\cdot\mathbf{t}$.

For enforcing the irreversibility condition for crack healing, another assumption is made in [11] by introducing a history variable $H = max_{\tau=[0,t_{max}]}[2l_0\psi(\boldsymbol{\varepsilon}(\mathbf{p},\tau))/G_c]$; where $\mathbf{p}$ is any point in the domain and τ is the respective timestep. By replacing the history variable in the Eq. (9), we reach the final governing equation for the fourth-order PF model

$$(H+1)\phi - \frac{l_0^2}{2}\Delta\phi + \frac{l_0^4}{16}\Delta^2\phi = H. \tag{13}$$

The initial crack is introduced using the history field as a function of the closest distance $d(\mathbf{p}, l)$ from any point $\mathbf{p}$ in the domain to the line l as [23]

$$H_0(\mathbf{p}) = B\begin{cases}\dfrac{G_c}{2l_0}\left(1 - \dfrac{2d(\mathbf{p},l)}{l_0}\right) d(\mathbf{p},l) \le \dfrac{l_0}{2} \\ 0 d(\mathbf{p},l) > \dfrac{l_0}{2}\end{cases}, where B = \frac{1}{1-\phi}, \tag{14}$$

we used $\phi = 1 - 10^{-3}$ to get the scalar parameter $B = 10^3$ for all the simulations.

By minimising the Eq. (5), writing it in 1D, and assuming $\phi(0) = 1$, $\frac{\partial\phi(0)}{\partial x} = 1[m^{-1}]$, $lim_{x\to\pm\infty}\frac{\partial\phi(x)}{\partial x} = 0[m^{-1}]$ and $lim_{x\to\pm\infty}\frac{\partial^2\phi(x)}{\partial x^2} = 0[m^{-2}]$ we get the homogeneous ordinary differential equation,

$$\phi(x) - \frac{l_0^2}{2}\frac{\partial^2\phi(x)}{\partial x^2} + \frac{l_0^4}{16}\frac{\partial^4\phi(x)}{\partial x^4} = 0. \tag{15}$$

The diffused crack for 1D at $x = 0[m]$ [4] can be derived by solving

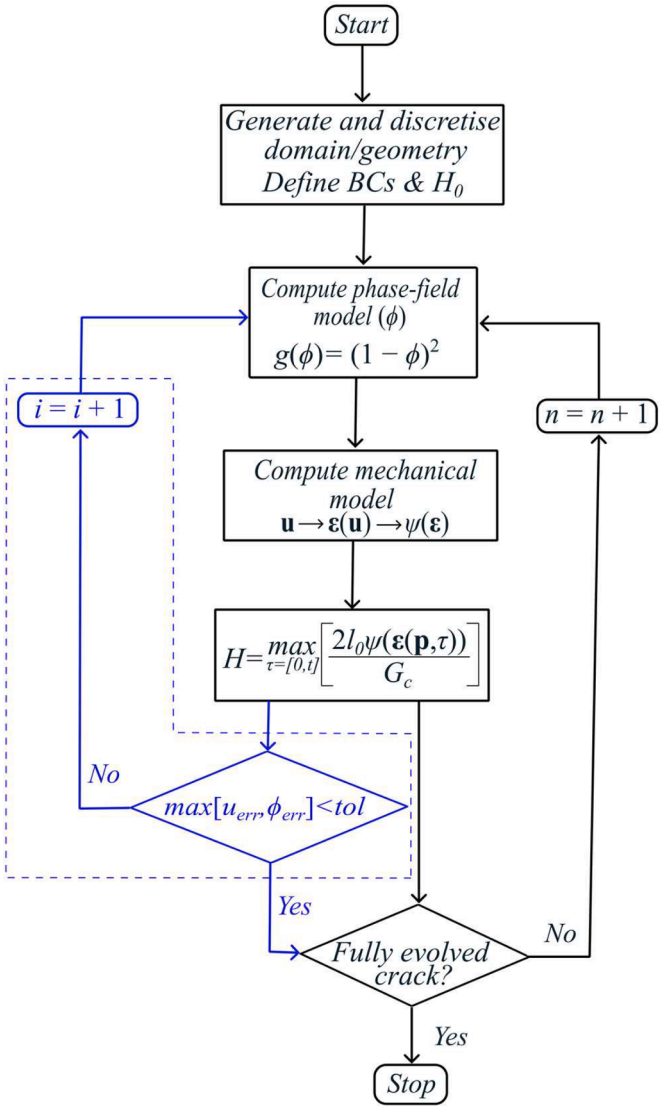

Fig. 3. Scheme of the solution procedure. The dotted lines surround the iterative process.

the Eq. (15) as

$$\phi(x)=\mathrm{e}^{\left(-\frac{|2x|}{l_0}\right)}\left(1+\frac{|2x|}{l_0}\right). \tag{16}$$

The effects of l_0 for a crack at $x=0[m]$ using the Eq. (16) are shown in Fig. 1. The diffused crack topology approaches the sharp crack topology as $l_0\rightarrow 0[m]$, as shown in Fig. 1.

3. Numerical method and solution procedure

The PFM and mechanical models are solved by the LRBFCM [54]. In LRBFCM, the domain Ω is divided into local subdomains ${}_l\Omega$, as shown in Fig. 2, and any function f is approximated numerically as

$${}_lf(\mathbf{p})\approx\sum_{i=1}^{{}_lN}{}_l\alpha_{il}\Phi_i(\mathbf{p}), \tag{17}$$

where the index i runs over ${}_lN$ local nodes of the ${}_l\Omega$ and ${}_l\alpha_i$ represents the unknown coefficients to be determined by collocation and ${}_l\Phi_i(\mathbf{p})$ are the shape functions. In order to overcome the ill-conditioning of the local interpolation problem, the augmented RBFs are used as

$${}_lf(\mathbf{p})\approx\sum_{i=1}^{{}_lN}{}_l\alpha_{il}\Phi_i(\mathbf{p})+\sum_{i=1}^{M}{}_l\alpha_{({}_lN+i)}p_i(\mathbf{p})=\sum_{i=1}^{{}_lN+M}{}_l\alpha_{il}\Psi_i(\mathbf{p}), \tag{18}$$

where p_i represents the monomials ($p_1=1$, $p_2=x$, $p_3=y$, $p_4=x^2$,$p_5=xy$, $p_6=y^2$) and ${}_l\Psi_i(\mathbf{p})$,$i=1,\ldots.,{}_lN+M$ describes the augmented shape functions with $M=6$ is the number of monomials.

Any differential equation with a linear differential operator L, using the Eq. (18), can be written as

$$L_lf(\mathbf{p})=\sum_{\chi=1}^{n_d}L_\chi f_\chi(\mathbf{p})\approx\sum_{\chi=1}^{n_d}\sum_{i=1}^{{}_lN+M}{}_l\alpha_{i,\chi}L_\chi{}_l\Psi_i(\mathbf{p}), \tag{19}$$

where n_d is the space dimension, the constants ${}_l\alpha_{i,\chi}$ are calculated from the Eq. (19) through a linear system of equations as $\mathbf{Ax}=\mathbf{b}$, where $\mathbf{A}$ is the sparse matrix of known coefficients, $\mathbf{b}$ contains the right-hand side of the governing equation along the boundary conditions and $\mathbf{x}$ is a column matrix of unknown values. A detailed explanation of the methodology is presented in [55].

The PHSs are a particular type of RBF employed in the present work as shape functions ${}_l\Phi_i(\mathbf{p})$. The scaled PHS is defined as [55]

$${}_l\Phi_i(\mathbf{p})=\left(\frac{\|\,\mathbf{p}-{}_l\mathbf{p}_i\,\|}{{}_lh}\right)^m, \tag{20}$$

where $m=1,3,5,\ldots$ is the order of PHS, and in this article $m=3$, and ${}_lh$ is the scaling parameter, which is the average distance of the subdomain nodes from the central node, calculated as

$${}_lh=\sqrt{\sum_{i=2}^{{}_lN}\frac{\|\,{}_l\mathbf{p}-{}_l\mathbf{p}_i\,\|^2}{{}_lN-1}}. \tag{21}$$

The PF and mechanical models are solved in a staggered form, as proposed in [11], by solving PF with a frozen mechanical model and vice versa. The solution procedure is shown in Fig. 3. The crack is initialised with the history field using the Eq. (14). Once the history field is initiated, then we use this initial history field to compute the PF (ϕ). This study computes the PF by introducing an intermediate variable $\chi=\frac{l_0^2}{2}\Delta\phi$ to reduce the fourth-order of the original Eq. (13) into two second-order differential equations as

$$\frac{l_0^2}{2}\Delta\phi-\chi=0, \tag{22}$$

$$(H+1)\phi-\chi+\frac{l_0^2}{8}\Delta\chi=H. \tag{23}$$

An alternative to this process would be the recursive formulation proposed in [77], where higher-order derivatives are avoided using lower-order terms. The fourth-order differential equation requires higher-order basis functions, leading to larger local interpolation problems and a denser stiffness matrix as compared to the second-order differential equation.

As soon as ϕ is computed, it is supplied to the mechanical model in terms of the degradation function $g(\phi)$, which degrades the material stiffness matrix. The mechanical model (Eq. (8)) is solved with a direct approach, as explained in [55]. The discretised form of the Eq. (8) in the direct approach is written as

$$[\nabla\cdot\mathbf{D}:\nabla^s+\mathbf{D}:\nabla\otimes\nabla^s]_n\mathbf{u}=-\mathbf{b}_n, \tag{24}$$

where $\mathbf{D}=g(\phi)\mathbf{C}$ is the degraded elasticity tensor, ∇^s is the symmetric gradient operator, n is the loading step. The resulting system of linear equations is solved for the displacement vector $\mathbf{u}$.

The respective operators in the Eq. (24) can be written in a matrix form as

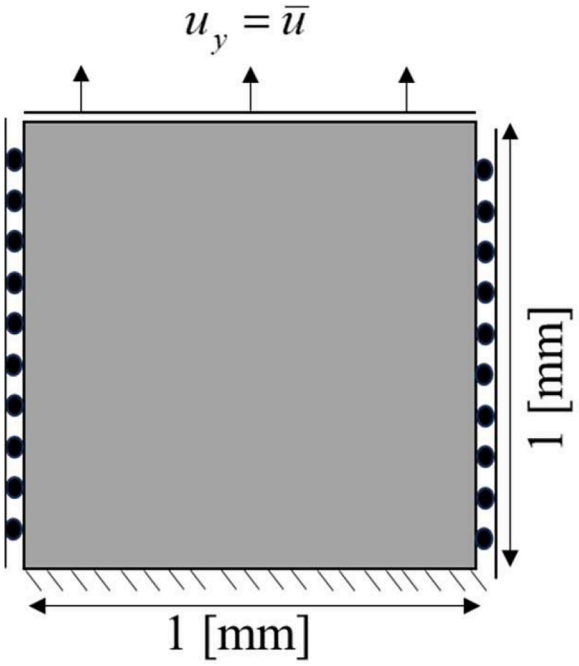

Fig. 4. Geometry and boundary conditions for a non-cracked square plate model subjected to uniaxial tension.

$$\nabla\cdot = \begin{bmatrix} \frac{\partial}{\partial x} & 0 & 0 & \frac{\partial}{\partial y} \\ 0 & \frac{\partial}{\partial y} & 0 & \frac{\partial}{\partial x} \end{bmatrix}, \mathbf{D} = g(\phi)\begin{bmatrix} \lambda+2\mu & \lambda & \lambda & 0 \\ \lambda & \lambda+2\mu & \lambda & 0 \\ \lambda & \lambda & \lambda+2\mu & 0 \\ 0 & 0 & 0 & 2\mu \end{bmatrix}, \nabla^s = \begin{bmatrix} \frac{\partial}{\partial x} & 0 \\ 0 & \frac{\partial}{\partial y} \\ 0 & 0 \\ \frac{\partial}{\partial y} & \frac{\partial}{\partial x} \end{bmatrix}$$

The degraded elasticity tensor is calculated for each point in the domain, and then the divergence operators, obtained from the RBFs with PHSs as shape functions, are applied to differentiate the material tensor. For the staggered solution with internal iterations (called iterative process in this study), a convergence check is required by calculating the L2 norm as

$$u_{err} = \frac{\| \mathbf{u}_{i+1} - \mathbf{u}_i \|}{\| \mathbf{u}_{i+1} \|}, \quad \phi_{err} = \frac{\| \phi_{i+1} - \phi_i \|}{\| \phi_{i+1} \|}, \tag{25}$$

where i is the number of iterations, and the iterative process continues till the criterion $max[u_{err},\phi_{err}] \leq tol$ is met. The solution with an iterative process is shown with the blue colour inside the box with dotted lines in Fig. 3, where the tolerance used is $tol = 10^{-4}$. In this study, the procedure where no internal iterations are utilised is termed a non-iterative process. The non-iterative process is also shown outside the dotted lines in Fig. 3.

The strain tensor is then calculated from the resulting displacements using the LRBFCM, and the strain energy density $\psi(\boldsymbol{\varepsilon})$ is calculated from the strain tensor, which is then used to update the initial history field. The updated history field is then supplied to the PFM, and this exchange of the computed fields continues until the material fails.

The method's numerical implementation is done using Julia version 1.8.0, where the coefficient matrix weights were calculated from the in-house built library. All the simulations were carried out using the 11th-generation Intel(R) Core(TM) i7–1165G7 @ 2 × 2.80 GHz processor.

4. Numerical examples

4.1. Non-cracked square plate model

A simple benchmark test with a non-cracked square plate geometry is considered to validate the LRBFCM implementation of PFM. The analytical solution to the problem in the Eqs. (26)-(29) are calculated by considering the boundary conditions $\varepsilon_{yy} \neq 0$, $\varepsilon_{xx} = \varepsilon_{xy} = 0$.

$$\sigma_{yy,0} = \frac{E(1-\nu)}{(1+\nu)(1-2\nu)}\varepsilon_{yy}, \tag{26}$$

$$\psi = \frac{1}{2}\frac{E(1-\nu)}{(1+\nu)(1-2\nu)}\varepsilon_{yy}^2, \tag{27}$$

$$\phi = \frac{2\psi}{\frac{G_c}{l_0}+2\psi}, \tag{28}$$

$$\sigma_{yy} = (1-\phi)^2\sigma_{yy,0}, \tag{29}$$

where σ_{yy} and ε_{yy} are the axial stress and axial strain respectively. The geometry and boundary conditions are shown in Fig. 4, with a tensile loading applied on the top edge. The material properties are chosen as: $E = 210kN/mm^2$, $\nu = 0.3, G_c = 0.005kN/mm$ and $l_0 = 0.1mm$. The

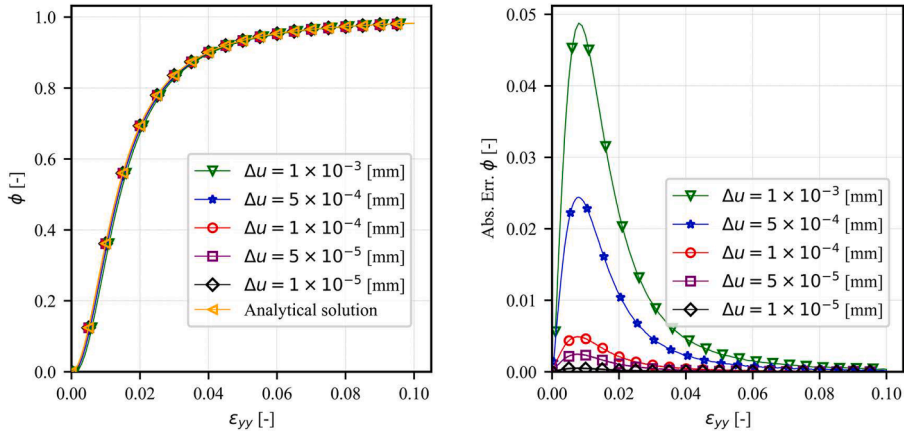

Fig. 5. Non-iterative process: The left side compares analytical and numerical solutions for PF and the right side the absolute error as a function of ε_{yy} using different loading steps.

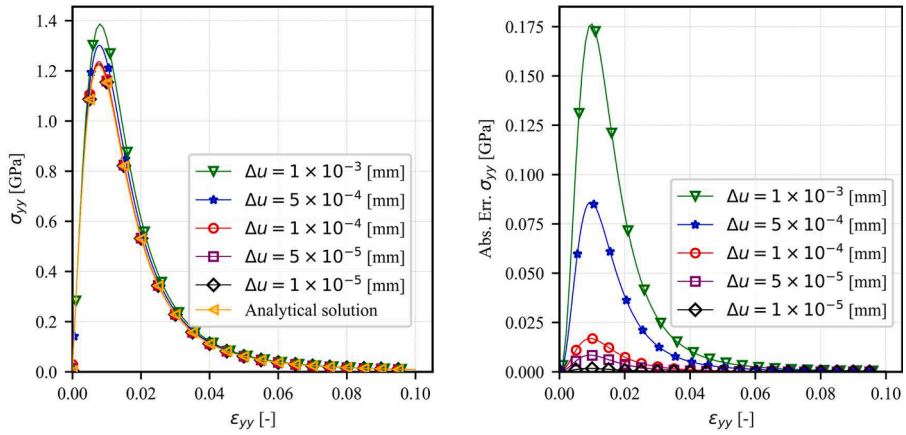

Fig. 6. Non-iterative process: The left side compares analytical and numerical solutions for σ_{yy} and the right side the absolute error as a function of ε_{yy} using different loading steps.

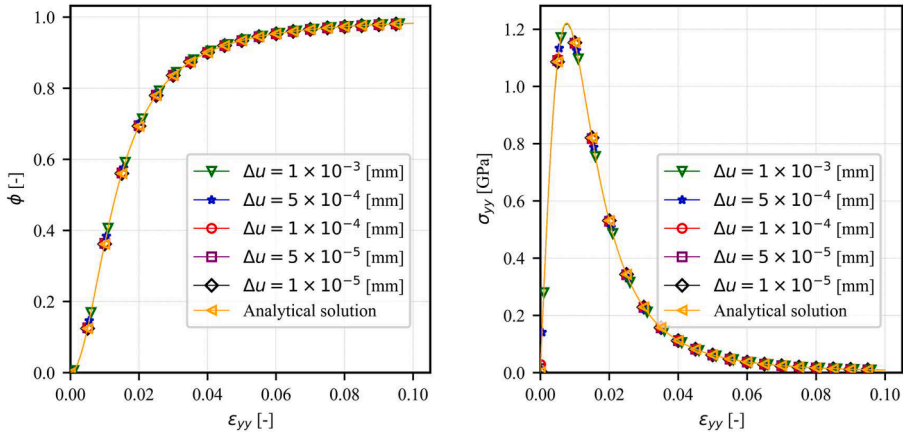

Fig. 7. Iterative process: The left side compares analytical and numerical solutions for PF and the right side compares σ_{yy} as a function of ε_{yy} using different loading steps.

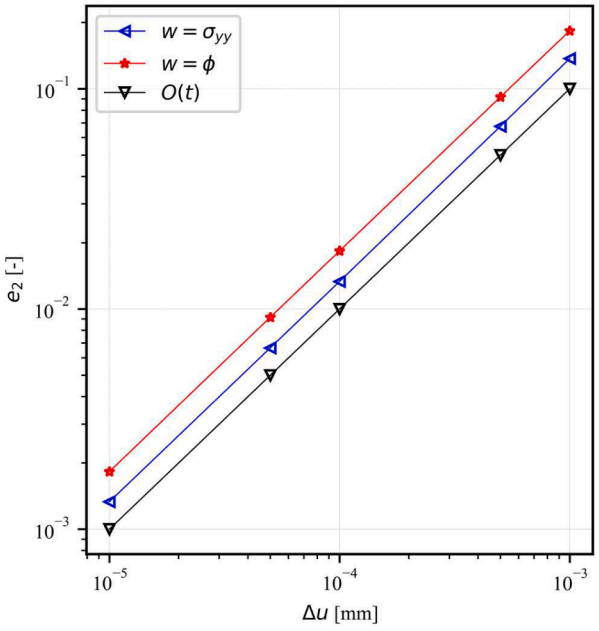

Fig. 8. Convergence in terms of loading steps: error as a function of loading steps at $\varepsilon_{yy} = 0.008$ **[mm]**.

numerical parameters are $h = 0.005[mm]$ (regular node distribution) with ${}_lN = 13$ and $M = 6$. The simulations are carried out using different loading steps to show the dependence of the staggered solution (with and without any iterations) on the size of the loading step Δu.

4.1.1. Comparison of numerical and analytical solutions with the non-iterative process

In this section, the simulations are carried out with a non-iterative process, and a subsequent loading increment is applied immediately after each staggered (mechanical model and PFM) step. The PF and its absolute error are shown as a function of axial strain on the left and right sides of Fig. 5, respectively. The axial stress and its absolute error are shown as a function of axial strain on the left and right sides of Fig. 6, respectively. As shown in Fig. 5 and Fig. 6, five different loading steps are chosen to see the dependence of the solution on the size of the loading step. It is clear from the figures that as we decrease the size of the loading step, the error decreases, and the numerical solution approaches the analytical solution. The most accurate results are for the loading step $\Delta u = 1 \times 10^{-5}$, while the least accurate results are for the loading step $\Delta u = 1 \times 10^{-3}$.

4.1.2. Comparison of numerical and analytical solutions with iterative process

The comparison of the numerical and analytical solutions with an intermediate iterative process for PF and axial stress is shown on the left-hand and right-hand sides of Fig. 7, respectively. It is clear from these

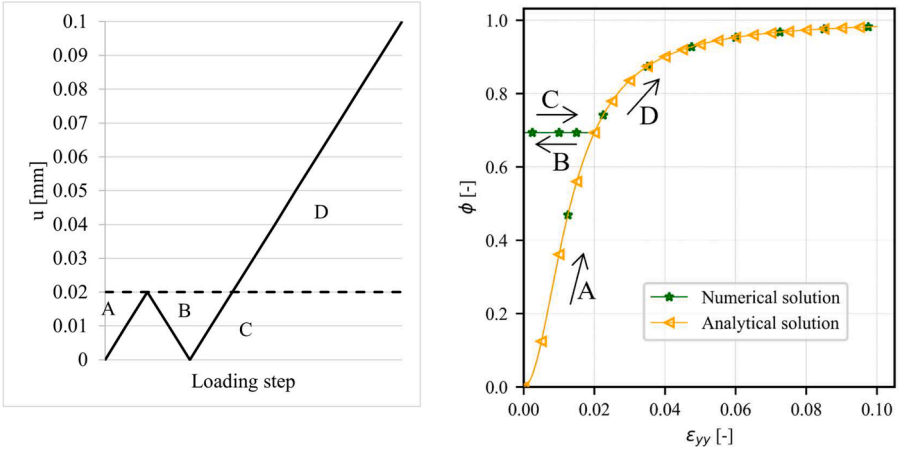

Fig. 9. The left side shows the applied displacement as a function of the loading step, and the right side shows the PF as a function of ε_{yy}.

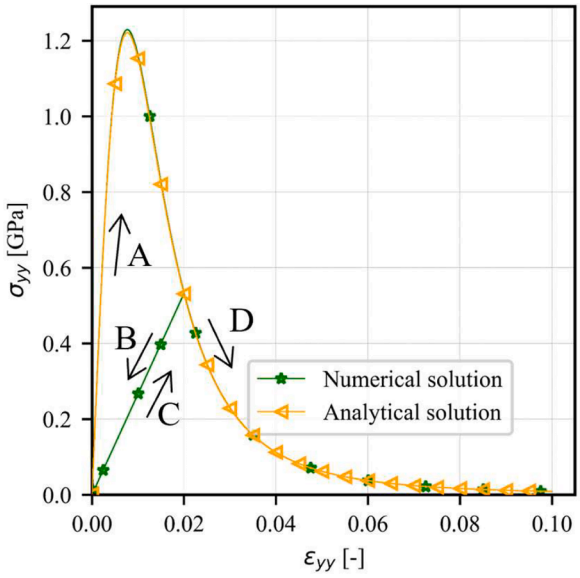

Fig. 10. σ_{yy} as a function of ε_{yy} with the applied loading.

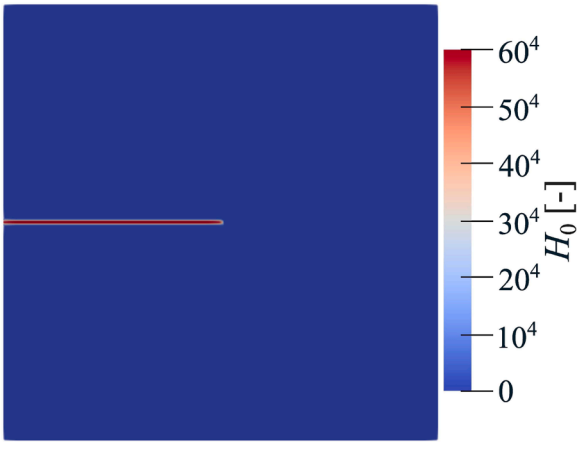

Fig. 11. Initial history field.

figures that if the iterative process is adopted, then the numerical solutions fall on the analytical solution irrespective of the loading step. If small enough loading steps are used, even with a non-iterative process, this error becomes insignificant, as shown for the loading step $\Delta u = 1 \times 10^{-5}$ in Fig. 5 and Fig. 6.

4.1.3. Convergence of the solution in terms of loading step

In this section, the convergence of the solution in terms of the loading step, with a non-iterative process, is shown in Fig. 8. The error e_2 is calculated as shown in the Eq. (30).

$$e_2 = \frac{|w - \widehat{w}|}{|\widehat{w}|}, \tag{30}$$

where w is the numerical solution and $\widehat{w}$ is the analytical solution. The solution for PF and stress shows a first-degree convergence rate, as shown in Fig. 8. The straight line $O(t)$ shows the first-degree convergence rate. Therefore, the smaller the loading step, the higher the accuracy.

4.1.4. Validation of the enforced irreversibility condition in terms of loading and unloading

The implementation of the enforced irreversibility condition (no healing of the crack) is checked by the loading shown on the left side of Fig. 9. The evolution of PF is shown on the right side of Fig. 9, whereas the relation between axial stress and axial strain is shown in Fig. 10. The PF increases as the loading is increased (step A), but there is no change in PF as the material is unloaded (step B) and subsequently loaded (step C). There is no change in PF during unloading, and the reload is due to the enforcement of the irreversibility condition in the history field. As soon as the history field increases (step D), the PF evolves again and reaches the value one (completely broken state). Fig. 8 shows that as the PF evolves, the axial stress decreases. The stress reduces and approaches zero during the unloading step (step B). Still, as soon as the material is loaded again (step C), the stress increases, following the same path it followed during the unloading. When the PF starts evolving again (step D), the axial stress decreases again and eventually reaches the value of approximately equal to zero (breaking the material).

4.2. A single-edge cracked square plate subjected to tensile loadings

The second benchmark test considered is the well-known single-edge cracked square plate subjected to tensile loadings. The geometry and boundary conditions are the same as shown in Fig. 4 where the initial history field is shown in Fig. 11. The geometry is fixed at the bottom in both x and y directions, and a load at increment n is defined for u_y on the top boundary as $\overline{u}_n = \overline{u}_{n-1} + \Delta u$. Where a variable loading increment is applied, that is $\Delta u = 1 \times 10^{-5}[mm] if n \leq 450$, otherwise, the loading increment is adjusted to $\Delta u = 1 \times 10^{-6}[mm]$ until the failure of the material. The material properties are chosen to be $\lambda = 121.15 \times$

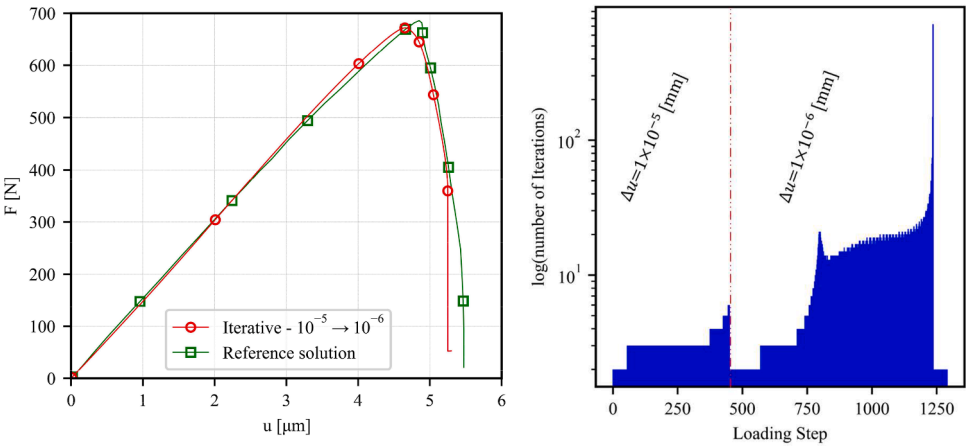

Fig. 12. The left side compares the force-displacement curve for the solution with the reference solution, and the right side shows the number of iterations required for each loading step.

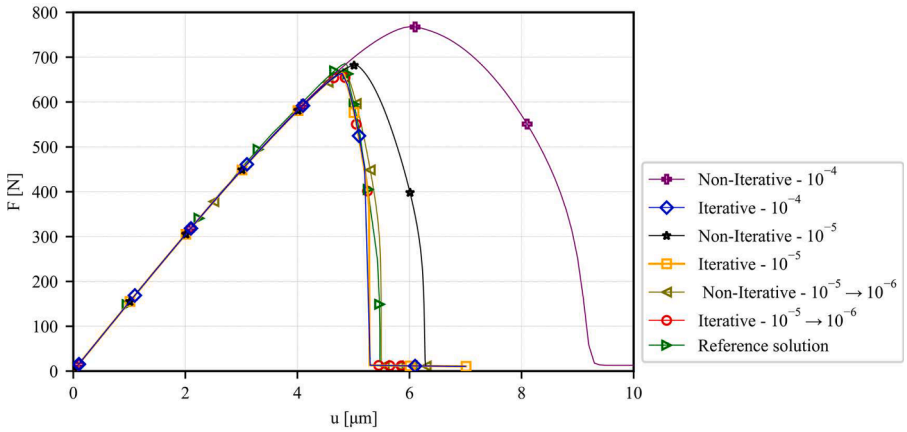

Fig. 13. Force-displacement graph for different loading step sizes with iterative and non-iterative schemes.

Table 1
Total iterations required for the respective loading step size.

Δu [mm]	Total iterations	Peak load [N]	CPU time [hr]
(Constant increment) 1×10^{-4}	2277	664.05	4.86
(Constant increment) 1×10^{-5}	7483	664.13	15.96
(Variable increment) $1 \times 10^{-5} \rightarrow 1 \times 10^{-6}$	11,793	664.20	25.15

$10^3[N/mm^2]$, $\mu = 80.77 \times 10^3[N/mm^2]$, $G_c = 2.7[N/mm]$ and $l_0 = 0.015[mm]$ to match with the material properties in the reference [22]. The numerical parameters are $h = 0.0075[mm]$ (regular node distribution) with total nodes $N = 18225$, $N = 13$, $M = 6$. Unless otherwise stated, these simulation parameters and material properties are used in all the simulations.

4.2.1. Model verification with the reference solution

A comparison of the results with the reference solution [22] is shown in Fig. 12. In this example, an iterative process for the staggered solutions of the PF and mechanical models is used. In the iterative process, after applying the first loading increment and computing the PF and mechanical models, another loading increment is applied when the error norm is less than the prescribed error in both PF and displacement fields. The force-displacement curve is shown on the right side of Fig. 12. It is clear from this figure that the results of the present study agree with the reference solution. The right side of Fig. 12 shows the number of

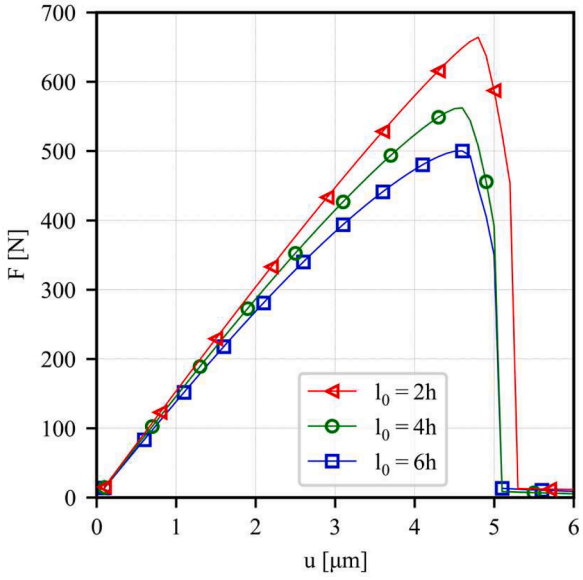

Fig. 14. Force-displacement graph at different length scale parameters.

Table 2
Minimum node spacing and the respective l_0/h ratio in different cases.

Case	h [mm]	l_0 [mm]	l_0/h
1	0.02	0.04	2
2	0.01	0.04	4
3	0.00666	0.04	6
4	0.005	0.04	8
Reference	0.004	0.04	10

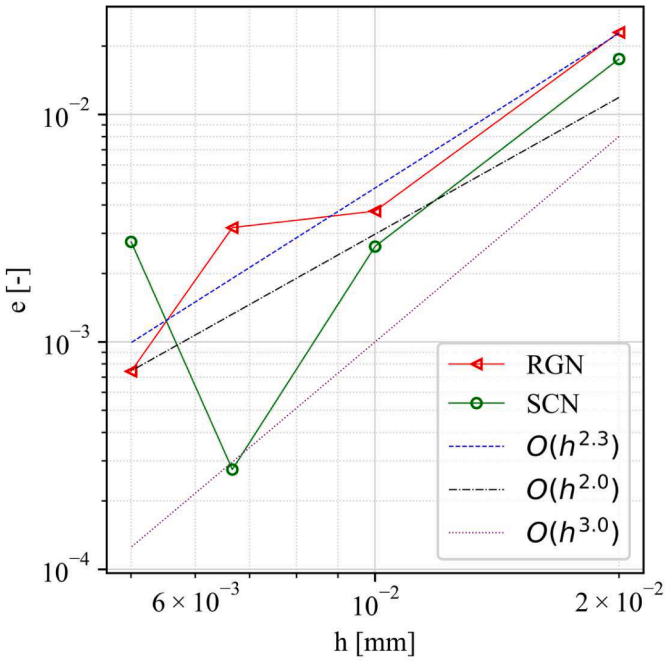

Fig. 15. Convergence in terms of the peak load for RGN and SCN with the respective rate of convergence.

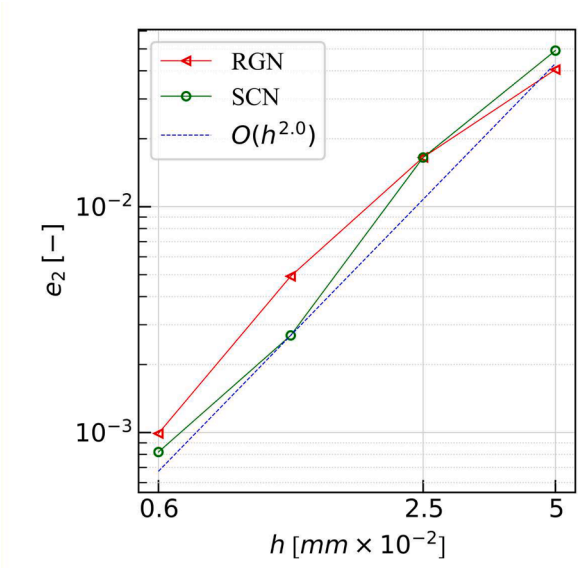

Fig. 16. Convergence in terms of displacement.

iterations required for each loading step, and a total of 11,769 iterations were needed until the complete failure of the material. Initially, the solution converges with a small number of iterations with a load increment $\Delta u = 1 \times 10^{-5}[mm]$, however, as soon as the simulations

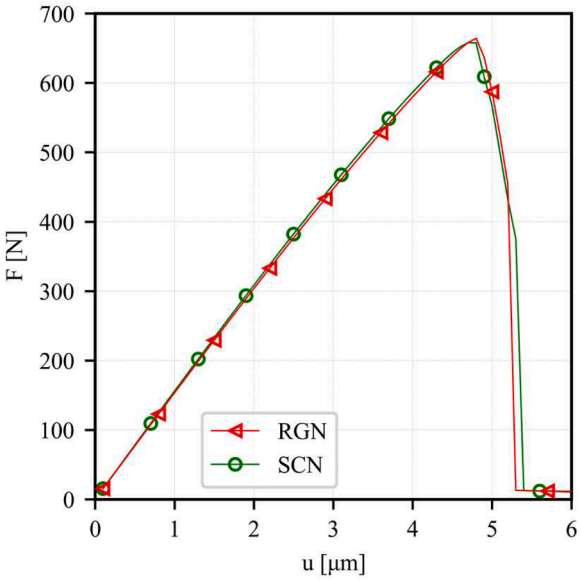

Fig. 17. Force-displacement graph for RGNs and SCNs.

Table 3
Total number of iterations required for RGN and SCN.

Δu [mm]	Total iterations	Peak load [N]	CPU time [hr]
1×10^{-4} (RGN)	2277	664.05	4.86
1×10^{-4} (SCN)	1534	657.93	3.77

proceed and the PF values increase, the number of iterations also increases. It is shown that as the loading step approaches the 450th loading step, the iterations increase but suddenly decrease as soon as they exceed the 450th loading step. This is because of the set loading conditions; as it exceeds the 450th loading step, the loading increment is adjusted to $\Delta u = 1 \times 10^{-6}[mm]$. The same pattern is shown again as soon as the PF starts evolving; the number of iterations increases until the material fails.

4.2.2. *Effects of the loading step size*

The PF analysis of the crack propagations can be done with or without the iterative process. The staggered solution with a non-iterative process does not consider any internal iterations between the PF and mechanical models during a loading step. It applies the loading increment after each step without looking for a convergence check, as shown in Fig. 3. The importance of the iterative process is shown in Fig. 13, where different simulations are done with constant loading increments of $\Delta u = 1 \times 10^{-4}[mm]$, $\Delta u = 1 \times 10^{-5}[mm]$ and variable loading increment by adjusting the loading increment from $\Delta u = 1 \times 10^{-5}[mm]$ to $\Delta u = 1 \times 10^{-6}[mm]$ when the loading step $n > 450$. The comparison of the iterative and non-iterative processes is shown in a force-displacement graph in Fig. 13. The solution with a non-iterative process with large loading steps possesses a high peak load, and the material behaviour is non-brittle. For example, using $\Delta u = 1 \times 10^{-4}[mm]$ with a non-iterative process, possesses a peak load of 767.7 [N], whereas the material breaks completely at a displacement of 0.0093 [mm].

In contrast, using an iterative process with the same loading step of $\Delta u = 1 \times 10^{-4}[mm]$, the material peak load is 664.05 [N], the complete breaking of the material occurs at a displacement of 0.0053 [mm], and as expected, the material behaviour is brittle. As the loading step is decreased to $\Delta u = 1 \times 10^{-5}[mm]$, the same trend is observed as in the case of $\Delta u = 1 \times 10^{-4}[mm]$, but the peak load for the non-iterative and iterative processes is reduced to 681.7 [N] and 664.13 [N] with a

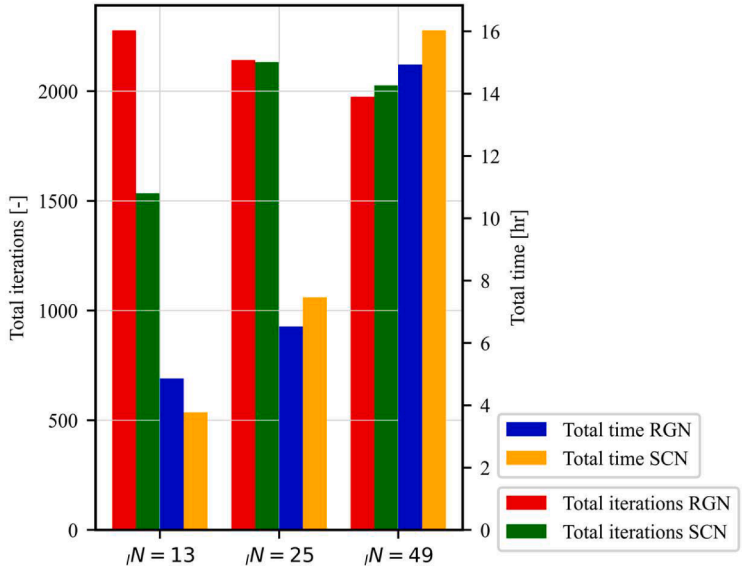

Fig. 18. The left and right vertical axis represents the total iterations and total time respectively as a function of the nodes in the local subdomain using RGNs and SCNs.

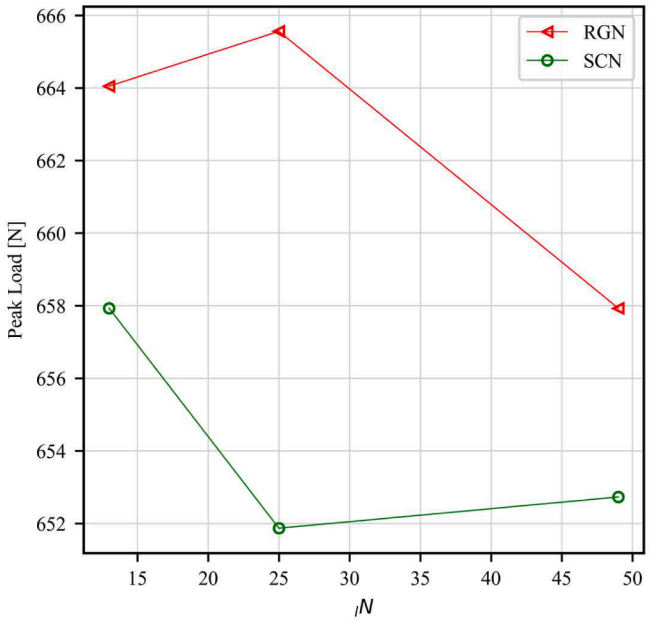

Fig. 19. Peak load as a function of the number of nodes in the local subdomain.

Table 4
Total iterations for different numbers of nodes in the local subdomain and the total CPU time with peak load for RGNs and SCNs.

$_lN$	Peak load [N]	Total iterations	Time/iteration [s]	CPU time [hr]
13 (SCN)	657.93	1534	8.87	3.77
13 (RGN)	664.05	2277	7.68	4.86
25 (SCN)	651.87	2132	12.60	7.46
25 (RGN)	665.56	2142	10.98	6.53
49 (SCN)	652.73	2026	28.50	16.03
49 (RGN)	657.93	1975	27.22	14.93

complete breaking of the material at a displacement of 0.0062 [mm] and 0.00528 [mm] respectively. In the non-iterative process, the material does not break immediately after the peak load is reached but instead breaks following a continuous smooth curve. As soon as the loading step size is adjusted from $\Delta u = 1 \times 10^{-5}[mm]$ to $\Delta u = 1 \times 10^{-6}[mm]$ the peak load for non-iterative and iterative processes, it decreased 666.17 [N] and 664.20 [N] with a complete failure of the material at a displacement of 0.0055 [mm] and 0.00528 [mm] respectively. The iterative process is used to speed up the simulation time, as shown in Fig. 15; even if a large loading step is used, the material breaks at the same displacement with a sharp and sudden crack, revealing the brittle behaviour of the material, after the peak load is reached. The comparison of the total number of iterations required for the respective loading step size is shown in Table 1 below. It is clear from Table 1 that a lading step size of $\Delta u = 1 \times 10^{-4}[mm]$ requires the least amount of iterations with comparable results compared to using a smaller loading step size, which is computationally efficient. In the remaining simulations, the loading step of $\Delta u = 1 \times 10^{-4}[mm]$ is used with an iterative process.

4.2.3. *Effects of the size of the length scale parameter*

The length scale parameter is essential for PF crack propagation because it measures the crack's width and diffusion. It has been shown in [76] that for a consistent PF crack propagation, $l_0 \geq 2h$, and $h = 0.0075$ $[mm]$ is the minimum node spacing. We consider three different values of l_0 as shown in Fig. 14. The value of the resulting peak load decreases as soon as the value of l_0 is increased. This is because a larger value of l_0 produces a more diffused PF, which in turn produces a more diffused degradation function. As a result, it softens the material more quickly, requiring a smaller force to break it.

4.2.4. *Effects of the node arrangement density*

In this section, the value of the length scale parameter is kept constant while the node arrangement density is gradually increased. An equal minimum node spacing is used in these simulations for both regular nodes (RGNs) and scattered nodes (SCNs) and is given in Table 2. The results were compared with the densest node arrangement ($h = 0.004$[mm]) by calculating the relative error for the peak load using the Eq. (31)

$$e = \frac{|a - \widehat{a}|}{|a|}, \tag{31}$$

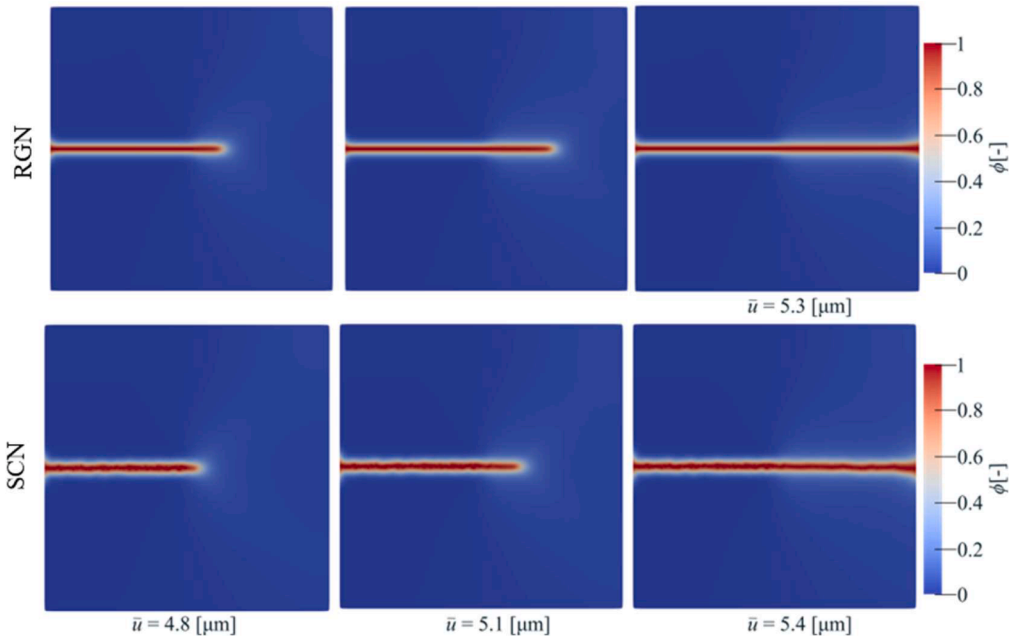

Fig. 20. PF evolution at different applied loadings with RGNs and SCNs.

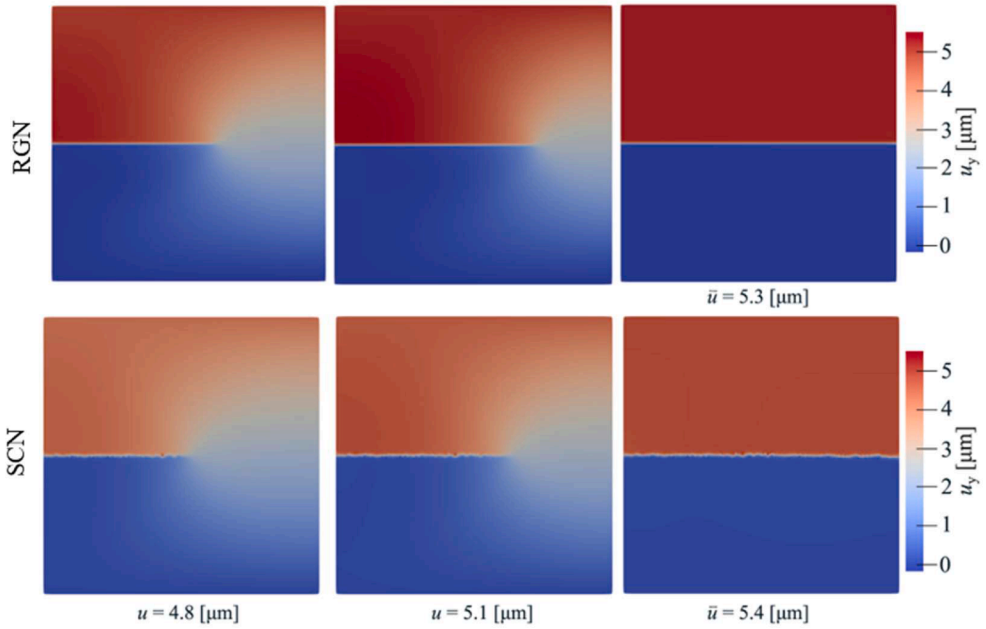

Fig. 21. Displacement field at different applied loadings with RGNs and SCNs.

where a is the peak load with the densest node arrangement (considered reference solution), and $\hat{a}$ is the peak load with the respective node arrangement. The results of the convergence study are shown in Fig. 15, where the relative error against the minimum node spacing is plotted. The straight lines in the figure represent the respective rates of convergence, denoted by $O(h^p)$, where h is the minimum node spacing and p is the convergence rate exponent.

The RGN exhibit a convergence rate of approximately $O(h^{2.3})$, indicating that the relative error decreases rapidly as the node spacing becomes finer. In contrast, the SCN shows a convergence rate of about $O(h^{2.0})$. Although this rate is slightly lower than that of RGN, it still reflects an exceptional improvement in accuracy with finer node spacing.

4.2.5. Convergence test for displacement in terms of node density

In this convergence test, a relative L_2 norm is calculated for the displacement field with different node densities. The reference solution is computed with the densest node arrangement having node spacing $h = 0.0031[\text{mm}]$. In order to satisfy the minimum l_0 criteria we have used $l_0 = 0.1[mm]$ in the simulations. The relative L_2 norm e_2 is calculated after the first loading step is applied

$$e_2 = \sqrt{\frac{\sum_i^N \| u_i - \hat{u}_i \|^2}{\sum_i^N \| \hat{u}_i \|^2}}, \tag{32}$$

where u represents the solution with less dense node arrangement and $\hat{u}$ is the reference solution. The convergence plot is shown in Fig. 16, where the relative error for both RGN and SCN is plotted against the

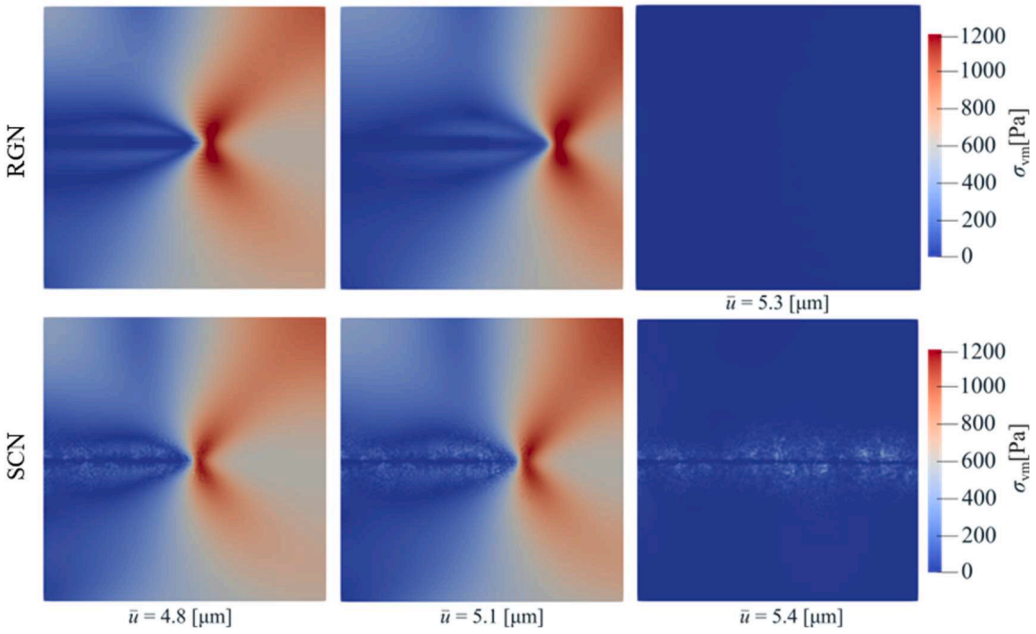

Fig. 22. Von Mises stress at different applied loadings with RGNs and SCNs.

node spacing. It can be seen that the rate of convergence is approximately equal to $O(h^{2.0})$, indicating a second-degree convergence rate governed by the order of augmentation.

4.2.6. Regular and scattered node distribution

The SCNs are extremely important in testing the method performance because, in real-world problems, the crack will not be explicitly defined, and for the LRBFCM, the PF crack propagation must work with the SCNs. Therefore, the LRBFCM is tested with both RGNs ($h = 0.0075$ $[mm]$) and SCNs ($h = 0.0075[mm]$), as shown in Fig. 17. The results for both RGN and SCN are in good agreement, showing that the method performs well with SCN. The complete failure of the material for RGN and SCN occurs at 0.0053 [mm] and 0.0054 [mm], respectively. The SCN performs better in terms of computational efficiency for this current case, with 13 nodes in the local subdomain, as shown in Table 3. SCN requires only 1534 iterations, while RGN requires 2277, showing that SCN is a good choice for better computational performance, where the difference in loading steps for the complete failure of the material while using RGN is one loading step less than that of SCN. The typical CPU time for both RGN and SCN is also shown in Table 3.

In order to check the trend for computational timing, three different simulations were conducted for ${}_{l}N = 13$, ${}_{l}N = 25 and {}_{l}N = 49$, as shown in Fig. 18. The respective total timing is shown on the right vertical axis of Fig. 18, and the respective peak loads against the number of nodes in the local subdomains are shown in Fig. 19. The respective values are also given in Table 4. It is clear from Fig. 18 that for ${}_{l}N = 13$, the SCN is a better choice for better computational efficiency, but as we increase the nodes in the local subdomain, then this trend does not remain the same. Therefore, the computational timing also depends on the simulation parameters; as the number of nodes in the local subdomain increases, the time for the completion of one iteration increases, as shown in Fig. 18 and Table 4. The peak loads for SCN are smaller than for RGN, as shown in Fig. 19.

The evolution of PF for both RGN and SCN is shown in Fig. 20, whereas the respective displacement and Von Mises stresses are shown in Fig. 21 and Fig. 22. The displacement field splits into two coloured regions, indicating a complete failure of the material. As soon as the material breaks, the respective Von Mises stresses become zero, showing that the material is no longer intact.

5. Conclusions

This article solves the phase field formulated crack propagation in a brittle elastic material using a strong-form meshless method for the first time. The PF and mechanical models are solved in a staggered form. The performance of the solution is analysed using two-dimensional benchmark tests. The first case consists of a non-cracked square plate model subjected to uniaxial tensile loadings to validate the implementation of PFM. The numerical solution with iterative and non-iterative processes are compared with the analytical solution. The results of the numerical solution, using the iterative process between two consecutive loading steps, converge to the analytical solution even if a large loading step is used. In contrast, with the non-iterative process, the error increases as the loading step increases and vice versa. A first-degree convergence rate is observed by decreasing the loading step against the error norm. In the last part of the first case, the implementation of the forced irreversibility is confirmed by loading and unloading the material. During the first loading stage, both the stresses and PF increased, but in the second unloading stage, due to the irreversibility condition, the PF remained constant, whereas the stresses became zero. In the third loading stage again, the PF and stresses followed the same curve as in the second stage but in the opposite direction. During the fourth stage, the material experienced a failure by the PF reaching a value of 1 and stresses reaching approximately equal to zero. This section proved that the PF implementation is correct, and the model is ready to proceed with the second test case.

The second test case consists of a single-edge cracked square plate subjected to tensile loadings. The obtained solution was compared with a good agreement with the FEM-based reference solution published in [22]. The effects of the loading step size with iterative and non-iterative processes are shown. It is concluded once again that the smaller the step size, the more accurate the results would be, but with a smaller loading step size, a large number of total iterations are required to break the material completely. On the other hand, with a non-iterative process, the material breaks unphysically (in a non-brittle manner) by reaching a very high peak load and breaking by following a smooth curve with a large displacement. Therefore, choosing an optimal step size and iterative process is necessary for proper accuracy and computational efficiency. The effects of the size of the length scale parameter are also studied, and it was found that increasing the value of the length scale

parameter with respect to the node spacing decreases the peak load and vice versa. A mesh convergence study is performed for both RGN and SCN; it is concluded that both RGN and SCN exhibit higher convergence rates, with RGN having a slightly higher convergence rate. At the end of the second test case, the simulations are performed using RGN and SCN, and it is shown that both RGNs and SCNs perform well for the specific case, and SCNs have better computational efficiency than RGNs with 13 nodes in the local subdomain. The results underline the essential role of the represented formulation structure for an accurate and efficient solution to crack propagation. It also provides valuable insights for future research towards three dimensions and more sophisticated material models.

CRediT authorship contribution statement

Izaz Ali: Writing – original draft, Visualization, Validation, Software, Resources, Methodology, Investigation, Formal analysis, Data curation, Conceptualization. **Gašper Vuga:** Writing – review & editing, Software, Resources, Methodology, Conceptualization. **Boštjan Mavrič:** Writing – review & editing, Software, Resources, Methodology, Conceptualization. **Umut Hanoglu:** Writing – review & editing, Resources, Methodology, Conceptualization. **Božidar Šarler:** Writing – review & editing, Supervision, Resources, Project administration, Methodology, Conceptualization.

Declaration of competing interest

The authors have no conflicts of interest to declare that are relevant to the content of this paper.

Acknowledgements

The Slovenian Research and Innovation Agency (ARIS) has supported this work in the framework of the Young Researcher Program, program group P2–0162, projects L2–3173, L2–2609, Z2–2640 and J2–4477, and Štore-Steel Company (www.store-steel.si). The authors would like to thank Prof. Jurica Sorić, Dr Tomislav Lesičar and Dr Hirshikesh for valuable discussions.

Data availability

No data was used for the research described in the article.

References

[1] Griffith AA. VI. The phenomena of rupture and flow in solids. Philos. Trans. R. Soc. Lond. Ser. Contain. Pap. Math. Phys. Character 1921;221(582–593):163–98. https://doi.org/10.1098/rsta.1921.0006.
[2] Zhuang X, Zhou S, Huynh GD, Areias P, Rabczuk T. Phase field modeling and computer implementation: a review. Eng. Fract. Mech. 2022;262:108234. https://doi.org/10.1016/j.engfracmech.2022.108234.
[3] Wu J-Y, Nguyen VP, Nguyen CT, Sutula D, Sinaie S, Bordas SPA. Phase-field modeling of fracture. Adv. Appl. Mech. 2020;53:1–183. https://doi.org/10.1016/bs.aams.2019.08.001.
[4] Goswami S, Anitescu C, Rabczuk T. Adaptive fourth-order phase field analysis for brittle fracture. Comput. Methods Appl. Mech. Eng. 2020;361:112808. https://doi.org/10.1016/j.cma.2019.112808.
[5] Lei J, Xu Y, Gu Y, Fan C-M. The generalized finite difference method for in-plane crack problems. Eng. Anal. Bound. Elem. 2019;98:147–56. https://doi.org/10.1016/j.enganabound.2018.10.016.
[6] Areias P, Msekh MA, Rabczuk T. Damage and fracture algorithm using the screened Poisson equation and local remeshing. Eng. Fract. Mech. 2016;158:116–43. https://doi.org/10.1016/j.engfracmech.2015.10.042.
[7] Bourdin B, Francfort GA, Marigo J-J. Numerical experiments in revisited brittle fracture. J. Mech. Phys. Solids 2000;48(4):797–826. https://doi.org/10.1016/S0022-5096(99)00028-9.
[8] T. Dobravec, "Numerical modelling of dendritic solidification based on phase field formulation and adaptive meshless solution procedure," University of Nova Gorica, Slovenia, 2021.
[9] Francfort GA, Marigo J-J. Revisiting brittle fracture as an energy minimization problem. J. Mech. Phys. Solids 1998;46(8):1319–42. https://doi.org/10.1016/S0022-5096(98)00034-9.
[10] Mumford D, Shah J. Optimal approximations by piecewise smooth functions and associated variational problems. Commun. Pure Appl. Math. 1989;42(5):577–685. https://doi.org/10.1002/cpa.3160420503.
[11] Miehe C, Welschinger F, Hofacker M. Thermodynamically consistent phase-field models of fracture: variational principles and multi-field FE implementations. Int. J. Numer. Methods Eng. 2010;83(10):1273–311. https://doi.org/10.1002/nme.2861.
[12] Li H, Wang W, Cao Y, Liu S. Phase-field modeling fracture in anisotropic materials. Adv. Civ. Eng. 2021;2021:1–13. https://doi.org/10.1155/2021/4313755.
[13] Nguyen-Thanh N, Li W, Huang J, Zhou K. Adaptive higher-order phase-field modeling of anisotropic brittle fracture in 3D polycrystalline materials. Comput. Methods Appl. Mech. Eng. 2020;372:113434. https://doi.org/10.1016/j.cma.2020.113434.
[14] De Borst R, Verhoosel CV. Gradient damage vs phase-field approaches for fracture: similarities and differences. Comput. Methods Appl. Mech. Eng. 2016;312:78–94. https://doi.org/10.1016/j.cma.2016.05.015.
[15] Sargado JM, Keilegavlen E, Berre I, Nordbotten JM. High-accuracy phase-field models for brittle fracture based on a new family of degradation functions. J. Mech. Phys. Solids 2018;111:458–89. https://doi.org/10.1016/j.jmps.2017.10.015.
[16] Ambati M, Gerasimov T, De Lorenzis L. A review on phase-field models of brittle fracture and a new fast hybrid formulation. Comput. Mech. 2015;55(2):383–405. https://doi.org/10.1007/s00466-014-1109-y.
[17] Novelli L, Gori L, da RL, Pitangueira Silva. Phase-field modelling of brittle fracture with Smoothed Radial Point Interpolation Methods. Eng. Anal. Bound. Elem. 2022;138:219–34. https://doi.org/10.1016/j.enganabound.2022.01.011.
[18] Shao Y, Duan Q, Qiu S. Adaptive consistent element-free Galerkin method for phase-field model of brittle fracture. Comput. Mech. 2019;64(3):741–67. https://doi.org/10.1007/s00466-019-01679-2.
[19] Hirshikesh, Pramod ALN, Annabattula RK, Ooi ET, Song C, Natarajan S. Adaptive phase-field modeling of brittle fracture using the scaled boundary finite element method. Comput. Methods Appl. Mech. Eng. 2019;355:284–307. https://doi.org/10.1016/j.cma.2019.06.002.
[20] Hirshikesh, Natarajan S, Annabattula RK. A FEniCS implementation of the phase field method for quasi-static brittle fracture. Front. Struct. Civ. Eng. 2019;13(2):380–96. https://doi.org/10.1007/s11709-018-0471-9.
[21] Wu J-Y. A unified phase-field theory for the mechanics of damage and quasi-brittle failure. J. Mech. Phys. Solids 2017;103:72–99. https://doi.org/10.1016/j.jmps.2017.03.015.
[22] Zhou S, Zhuang X. Adaptive phase field simulation of quasi-static crack propagation in rocks. Undergr. Space 2018;3(3):190–205. https://doi.org/10.1016/j.undsp.2018.04.006.
[23] Borden MJ, Verhoosel CV, Scott MA, Hughes TJR, Landis CM. A phase-field description of dynamic brittle fracture. Comput. Methods Appl. Mech. Eng. 2012;217–220:77–95. https://doi.org/10.1016/j.cma.2012.01.008.
[24] Hofacker M, Miehe C. Continuum phase field modeling of dynamic fracture: variational principles and staggered FE implementation. Int. J. Fract. 2012;178(1–2):113–29. https://doi.org/10.1007/s10704-012-9753-8.
[25] Ambati M, Gerasimov T, De Lorenzis L. Phase-field modeling of ductile fracture. Comput. Mech. 2015;55(5):1017–40. https://doi.org/10.1007/s00466-015-1151-4.
[26] Borden MJ, Hughes TJR, Landis CM, Anvari A, Lee IJ. A phase-field formulation for fracture in ductile materials: finite deformation balance law derivation, plastic degradation, and stress triaxiality effects. Comput. Methods Appl. Mech. Eng. 2016;312:130–66. https://doi.org/10.1016/j.cma.2016.09.005.
[27] Seleš K, Aldakheel F, Tonković Z, Sorić J, Wriggers P. A general phase-field model for fatigue failure in brittle and ductile solids. Comput. Mech. 2021;67(5):1431–52. https://doi.org/10.1007/s00466-021-01996-5.
[28] Ambati M, Kruse R, De Lorenzis L. A phase-field model for ductile fracture at finite strains and its experimental verification. Comput. Mech. 2016;57(1):149–67. https://doi.org/10.1007/s00466-015-1225-3.
[29] Nguyen-Thanh N, Li W, Huang J, Zhou K. Multi phase-field modeling of anisotropic crack propagation in 3D fiber-reinforced composites based on an adaptive isogeometric meshfree collocation method. Comput. Methods Appl. Mech. Eng. 2022;393:114794. https://doi.org/10.1016/j.cma.2022.114794.
[30] Msekh MA, et al. Predictions of J integral and tensile strength of clay/epoxy nanocomposites material using phase field model. Compos. Part B Eng. 2016;93:97–114. https://doi.org/10.1016/j.compositesb.2016.02.022.
[31] Dsouza SM, Hirshikesh, Mathew TV, Singh IV, Natarajan S. A non-intrusive stochastic phase field method for crack propagation in functionally graded materials. Acta Mech 2021;232(7):2555–74. https://doi.org/10.1007/s00707-021-02956-z.
[32] Khalil Z, Elghazouli AY, Martínez-Pañeda E. A generalised phase field model for fatigue crack growth in elastic–plastic solids with an efficient monolithic solver. Comput. Methods Appl. Mech. Eng. 2022;388:114286. https://doi.org/10.1016/j.cma.2021.114286.
[33] Lo Y-S, Borden MJ, Ravi-Chandar K, Landis CM. A phase-field model for fatigue crack growth. J. Mech. Phys. Solids 2019;132:103684. https://doi.org/10.1016/j.jmps.2019.103684.
[34] Martínez-Pañeda E, Golahmar A, Niordson CF. A phase field formulation for hydrogen assisted cracking. Comput. Methods Appl. Mech. Eng. 2018;342:742–61. https://doi.org/10.1016/j.cma.2018.07.021.
[35] Golahmar A, Kristensen PK, Niordson CF, Martínez-Pañeda E. A phase field model for hydrogen-assisted fatigue. Int. J. Fatigue 2022;154:106521. https://doi.org/10.1016/j.ijfatigue.2021.106521.

[36] Wu J-Y, Mandal TK, Nguyen VP. A phase-field regularized cohesive zone model for hydrogen assisted cracking. Comput. Methods Appl. Mech. Eng. 2020;358:112614. https://doi.org/10.1016/j.cma.2019.112614.
[37] Nguyen VP, Rabczuk T, Bordas S, Duflot M. Meshless methods: a review and computer implementation aspects. Math. Comput. Simul. 2008;79(3):763–813. https://doi.org/10.1016/j.matcom.2008.01.003.
[38] Borden MJ, Hughes TJR, Landis CM, Verhoosel CV. A higher-order phase-field model for brittle fracture: formulation and analysis within the isogeometric analysis framework. Comput. Methods Appl. Mech. Eng. 2014;273:100–18. https://doi.org/10.1016/j.cma.2014.01.016.
[39] Aurojyoti P, Rajagopal A. Fourth order phase field modeling of brittle fracture by natural element method. Int. J. Fract. 2024. https://doi.org/10.1007/s10704-024-00773-8.
[40] Nguyen KD, E.Augarde C, Coombs WM, Nguyen-Xuan H, Abdel-Wahab M. Non-conforming multipatches for NURBS-based finite element analysis of higher-order phase-field models for brittle fracture. Eng. Fract. Mech. 2020;235:107133. https://doi.org/10.1016/j.engfracmech.2020.107133.
[41] Prusty A, Rajagopal A. Modeling fracture in brittle materials by higher-order phase field method using C^1 non-Sibsonian interpolants. Eng. Comput. 2023;40(6):1508–41. https://doi.org/10.1108/EC-12-2022-0735.
[42] Ma R, Sun W. FFT-based solver for higher-order and multi-phase-field fracture models applied to strongly anisotropic brittle materials. Comput. Methods Appl. Mech. Eng. 2020;362:112781. https://doi.org/10.1016/j.cma.2019.112781.
[43] Svolos L, Mourad HM, Manzini G, Garikipati K. A fourth-order phase-field fracture model: formulation and numerical solution using a continuous/discontinuous Galerkin method. J. Mech. Phys. Solids 2022;165:104910. https://doi.org/10.1016/j.jmps.2022.104910.
[44] Franke M, Hesch C, Dittmann M. A HIGHER ORDER PHASE-FIELD APPROACH TO FRACTURE FOR FINITE-DEFORMATION CONTACT PROBLEMS. In: Proceedings of the VII European Congress on Computational Methods in Applied Sciences and Engineering (ECCOMAS Congress 2016). Crete Island, Greece: Institute of Structural Analysis and Antiseismic Research School of Civil Engineering National Technical University of Athens (NTUA) Greece; 2016. p. 6741–63. https://doi.org/10.7712/100016.2295.9907.
[45] Wu J, Wang D, Lin Z, Qi D. An efficient gradient smoothing meshfree formulation for the fourth-order phase field modeling of brittle fracture. Comput. Part. Mech. 2020;7(2):193–207. https://doi.org/10.1007/s40571-019-00240-5.
[46] Amiri F, Millán D, Arroyo M, Silani M, Rabczuk T. Fourth order phase-field model for local max-ent approximants applied to crack propagation. Comput. Methods Appl. Mech. Eng. 2016;312:254–75. https://doi.org/10.1016/j.cma.2016.02.011.
[47] Zhou S, Rabczuk T, Zhuang X. Phase field modeling of quasi-static and dynamic crack propagation: COMSOL implementation and case studies. Adv. Eng. Softw. 2018;122:31–49. https://doi.org/10.1016/j.advengsoft.2018.03.012.
[48] Zhou S, Zhuang X, Rabczuk T. A phase-field modeling approach of fracture propagation in poroelastic media. Eng. Geol. 2018;240:189–203. https://doi.org/10.1016/j.enggeo.2018.04.008.
[49] Navidtehrani Y, Betegón C, Martínez-Pañeda E. A unified abaqus implementation of the phase field fracture method using only a user material subroutine. Materials (Basel) 2021;14(8):1913. https://doi.org/10.3390/ma14081913.
[50] Msekh MA, Sargado JM, Jamshidian M, Areias PM, Rabczuk T. Abaqus implementation of phase-field model for brittle fracture. Comput. Mater. Sci. 2015;96:472–84. https://doi.org/10.1016/j.commatsci.2014.05.071.
[51] Seleš K, Lesičar T, Tonković Z, Sorić J. A residual control staggered solution scheme for the phase-field modeling of brittle fracture. Eng. Fract. Mech. 2019;205:370–86. https://doi.org/10.1016/j.engfracmech.2018.09.027.
[52] Molnár G, Gravouil A. 2D and 3D abaqus implementation of a robust staggered phase-field solution for modeling brittle fracture. Finite Elem. Anal. Des. 2017;130:27–38. https://doi.org/10.1016/j.finel.2017.03.002.
[53] Yu X, Wang R, Dong C, Ji J, Zhen X. 3D implementation of push-out test in ABAQUS using the phase-field method. J. Mech. Sci. Technol. 2023;37(4):1731–45. https://doi.org/10.1007/s12206-023-0314-z.
[54] Šarler B, Vertnik R. Meshfree explicit local radial basis function collocation method for diffusion problems. Comput. Math. Appl. 2006;51(8):1269–82. https://doi.org/10.1016/j.camwa.2006.04.013.
[55] G. Vuga, B. Mavrič, and B. Šarler, "An improved local radial basis function method for solving small-strain elasto-plasticity," 2023, doi: 10.48550/ARXIV.2308.03817.
[56] Saberi H, Nguyen CT, Saberi H, Sabagh M, Nguyen MN, Bui TQ. A computational meshfree RPIM approach for phase-field modeling of brittle fracture. Acta Mech 2024. https://doi.org/10.1007/s00707-024-03911-4.
[57] Wang H, Qin Q-H. Overview of meshless methods. Methods Fundamental Solution Solid Mech. 2019:3–51. https://doi.org/10.1016/B978-0-12-818283-3.00001-4. Elsevier.
[58] Tominec I, Larsson E, Heryudono A. A least squares radial basis function finite difference method with improved stability properties. SIAM J. Sci. Comput. 2021;43(2):A1441–71. https://doi.org/10.1137/20M1320079.
[59] Kansa EJ. Multiquadrics—a scattered data approximation scheme with applications to computational fluid-dynamics—I surface approximations and partial derivative estimates. Comput. Math. Appl. 1990;19(8–9):127–45. https://doi.org/10.1016/0898-1221(90)90270-T.
[60] Fu Z, Tang Z, Xi Q, Liu Q, Gu Y, Wang F. Localized collocation schemes and their applications. Acta Mech. Sin. 2022;38(7):422167. https://doi.org/10.1007/s10409-022-22167-x.
[61] Mavrič B, Šarler B. Equivalent-PDE based stabilization of strong-form meshless methods applied to advection-dominated problems. Eng. Anal. Bound. Elem. 2020;113:315–27. https://doi.org/10.1016/j.enganabound.2020.01.014.
[62] Mavrič B, Šarler B. Local radial basis function collocation method for linear thermoelasticity in two dimensions. Int. J. Numer. Methods Heat Fluid Flow 2015;25(6):1488–510. https://doi.org/10.1108/HFF-11-2014-0359.
[63] Kosec G, Šarler B. H-Adaptive local radial basis function collocation meshless method. Comput. Mater. Contin. 2011;26(3):227–54. https://doi.org/10.3970/cmc.2011.026.227.
[64] Hanoglu U, Šarler B. Multi-pass hot-rolling simulation using a meshless method. Comput. Struct. 2018;194:1–14. https://doi.org/10.1016/j.compstruc.2017.08.012.
[65] Vuga G, Mavrič B, Šarler B. Strong-form meshless numerical modelling of visco-plastic material. Eng. Analy. Boundary Elements (In print) 2024.
[66] Mramor K, Vertnik R, Šarler B. Simulation of laminar backward facing step flow under magnetic field with explicit local radial basis function collocation method. Eng. Anal. Bound. Elem. 2014;49:37–47. https://doi.org/10.1016/j.enganabound.2014.04.013.
[67] Ali I, Hanoglu U, Vertnik R, Šarler B. Assessment of Local Radial Basis Function Collocation Method for Diffusion Problems Structured with Multiquadrics and Polyharmonic Splines. Math. Comput. Appl. 2024;29(2):23. https://doi.org/10.3390/mca29020023.
[68] Flyer N, Fornberg B, Bayona V, Barnett GA. On the role of polynomials in RBF-FD approximations: I. Interpolation and accuracy. J. Comput. Phys. 2016;321:21–38. https://doi.org/10.1016/j.jcp.2016.05.026.
[69] Bayona V, Flyer N, Fornberg B, Barnett GA. On the role of polynomials in RBF-FD approximations: II. Numerical solution of elliptic PDEs. J. Comput. Phys. 2017;332:257–73. https://doi.org/10.1016/j.jcp.2016.12.008.
[70] Oruç Ö. A radial basis function finite difference (RBF-FD) method for numerical simulation of interaction of high and low frequency waves: zakharov–Rubenchik equations. Appl. Math. Comput. 2021;394:125787. https://doi.org/10.1016/j.amc.2020.125787.
[71] Bayona V, Flyer N, Fornberg B. On the role of polynomials in RBF-FD approximations: III. Behavior near domain boundaries. J. Comput. Phys. 2019;380:378–99. https://doi.org/10.1016/j.jcp.2018.12.013.
[72] Dobravec T, Mavrič B, Zahoor R, Šarler B. A coupled domain–boundary type meshless method for phase-field modelling of dendritic solidification with the fluid flow. Int. J. Numer. Methods Heat Fluid Flow 2023;33(8):2963–81. https://doi.org/10.1108/HFF-03-2023-0131.
[73] Vuga G, Mavrič B, Šarler B. A hybrid radial basis function-finite difference method for modelling two-dimensional thermo-elasto-plasticity, part 1: method formulation and testing. Eng. Anal. Bound. Elem. 2024;159:58–67. https://doi.org/10.1016/j.enganabound.2023.11.014.
[74] Vuga G, Mavrič B, Hanoglu U, Šarler B. A hybrid radial basis function-finite difference method for modelling two-dimensional thermo-elasto-plasticity, Part 2: application to cooling of hot-rolled steel bars on a cooling bed. Eng. Anal. Bound. Elem. 2024;159:331–41. https://doi.org/10.1016/j.enganabound.2023.12.001.
[75] Dobravec T, Mavrič B, Šarler B. Reduction of discretisation-induced anisotropy in the phase-field modelling of dendritic growth by meshless approach. Comput. Mater. Sci. 2020;172:109166. https://doi.org/10.1016/j.commatsci.2019.109166.
[76] Miehe C, Hofacker M, Welschinger F. A phase field model for rate-independent crack propagation: robust algorithmic implementation based on operator splits. Comput. Methods Appl. Mech. Eng. 2010;199(45–48):2765–78. https://doi.org/10.1016/j.cma.2010.04.011.
[77] Wang D, Wang J, Wu J. Arbitrary order recursive formulation of meshfree gradients with application to superconvergent collocation analysis of Kirchhoff plates. Comput. Mech. 2020;65(3):877–903. https://doi.org/10.1007/s00466-019-01799-9.